

How to calibrate edge sensors on segmented mirror telescopes

Chris Shelton, Lewis C Roberts, Jr.

Jet Propulsion Laboratory, California Institute of Technology, Pasadena CA 91109, USA

ABSTRACT

The next generation of large ground based telescopes use segmented mirrors. Sensors mounted on the edge of the segments measure the relative heights of the segments. The segments are actively controlled in height by three actuators per segment, but lateral motion is only passively constrained. Thus there will be some small change in the gap and shear between segments as changing telescope orientation and temperature make small distortions in the telescope structure. These "in-plane" motions place an additional performance burden on the edge sensors, and on the precision with which they must be mounted relative to the optical surface. In addition, both the scaling and offset of sensor edge height readings also vary with changes in gap.

Our method for correcting the in-plane motion induced errors in the primary mirror has three parts.

First, the edge sensors are modified to report segment-to-segment gap, as well as the height difference, to make the in-plane segment positions observable. Second, the mirror segments are phased optically, at a set of zenith angles and temperatures, to give a set of "measured sensor readings". Finally, during observing, a calibration procedure combines these data into "desired sensor readings" which are optimal for the current telescope state. We have included this calibration process in a control loop model of the Thirty Meter Telescope primary mirror control system. We present our calibration method and the model.

Keywords: Extremely Large Telescopes, edge sensors, segmented mirrors, capacitive sensor, calibration

1. INTRODUCTION

The largest monolithic optical telescopes have diameters of approximately 8m. Larger telescopes require the primary mirror to be segmented. To form a coherent image, the individual segments of the primary mirror need to be kept phased as wind, vibration, thermal changes and changing gravity vectors affect the relative segment positions. This is done through a control system, which takes sensor readings and then feeds back commands to a set of actuators that control the position of the individual segments.

There are a number of different sensor types that can be used in this servo loop; optical metrology, various types of wavefront sensors^{1,2,3} or edge sensors. Edge sensors measure the relative height, and possibly gap or shear between adjacent segments. These sensors appear on a number of current generation telescopes^{4,5,6} and are baselined on all of the next generation giant segmented mirror telescopes (GSMT): European Extremely Large Telescope⁷, Thirty Meter Telescope⁸ and the Giant Magellan Telescope⁹. Capacitive¹⁰, inductive¹¹ and optical¹² edge sensors have been designed. Each has its own performance and technical advantages.

The 492 hexagonal mirror segments that form the 30-meter TMT primary mirror (M1) must be precisely positioned with respect to each other to form a useful optical image. The M1 control system (M1CS) performs this task, with actuators that move segments in tip, tilt and piston relative to the mirror support structure^{13,14,15,16}. These movements are based on error signals generated from edge sensors that are exquisitely sensitive to the relative height and tilt of neighboring segments. In Figure 1, the blocks attached to the bottom edge of the hexagonal mirror are halves of edge sensors, with mating halves on neighboring segments^{4,10}.

While the segments are thus actively controlled in optical surface height, lateral motion is only passively constrained, by the backing structure. Thus there will be some small change in the gaps between segments, and some "shear" (segment-to-segment relative motion along an edge), as changing telescope orientation and temperature make small distortions in the steel backing structure.

These "in-plane" motions place an additional performance burden on the segment edge sensors, and on the precision with which they must be mounted relative to the optical surface.

A simple example illustrates the interaction between in-plane motion and sensor mounting tolerance. Consider ordinary thermal expansion of the M1 steel support structure compared to that of the Zerodur mirror segments. For TMT this thermal expansion difference by itself gives a change in the gap between segments of $14.4 \mu\text{m}/\text{C}$. If an edge sensor is mounted onto the mirror segments with a 1 mrad tilt, that edge sensor now has a $14.4 \text{ nm}/\text{C}$ height error, while the TMT requirement is for 1 nm/C or less, after calibration.

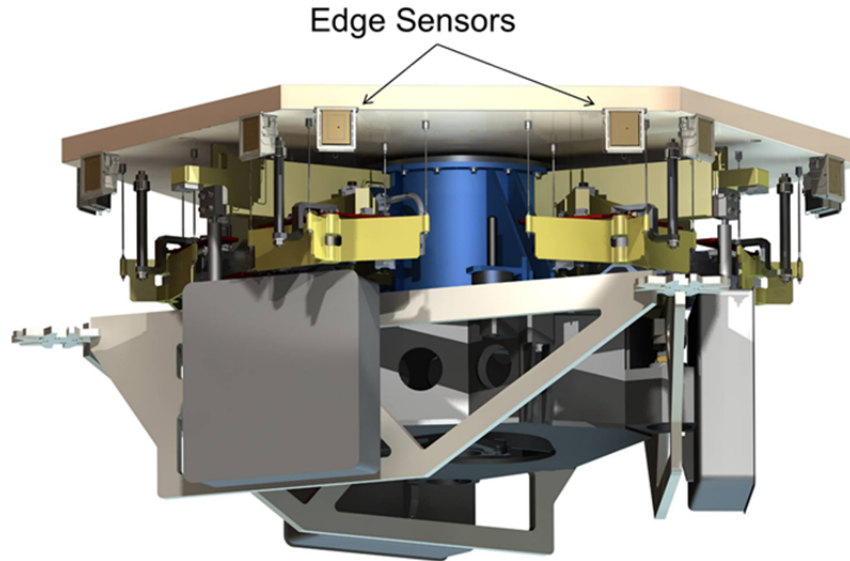


Figure 1. Close up view of a TMT Primary Segment Assembly attached to the mirror cell, showing the hexagonal mirror segment, three actuators, the warping harness, and some of the 12 edge sensors halves. The actuators are the large grey boxes.

In addition to this example of a purely geometric error, which is independent of sensor type, sensor edge height readings will also vary with changes in gap and with sensor tilts and rotations. The resulting errors are sensor-dependent, and more complex to analyze, but must also be compensated for to stay within the sensor error budget.

Our approach for correcting control system errors induced by in-plane motion in the primary mirror (M1) has three parts. First, the edge sensors are modified to report segment-to-segment gap, as well as their height difference, to provide knowledge of the in-plane segment positions. Second, the telescope is aligned, or “phased” on bright stars, at a sufficient set of zenith angles and temperatures. Third, a “calibration procedure” is applied which combines the results of the phasing runs into the coefficients of a correction formula.

In this paper, we will present this calibration procedure and its simulated operation on the Thirty Meter Telescope (TMT) M1 mirror control system (M1CS), and estimate its performance with practical levels of sensor mounting tolerances. The procedure is an extension and fleshing out of that proposed in 2006 by Mast, Nelson and Chanan¹⁰. The results of this simulation show that the TMT M1CS can meet its requirements with attainable sensor installation errors. Also, as other error sources have been identified, such as sensor sag with gravity, and sensor drift with temperature, the calibration procedure has proven robust against these too, without modification to the procedure.

2. TMT CAPACITIVE EDGE SENSORS

2.1 Segment control geometry

Figure 2 shows how actuators and sensors are distributed in the M1 active control geometry. Each segment has three actuators that move it as a rigid body, in tip, tilt and piston. Two edge sensors per common segment edge report on the relative position of neighboring segments. Each sensor has a drive half on one segment and a sense half on the other side of the gap between segments.

Each sensor has two output signals. An output called “height” actually is proportional to a combination of height difference and the dihedral angle between neighboring segments. The ratio of height to angle sensitivity is called the effective lever arm, or L_{eff} . Notice that the two sensors common to a neighboring pair of segments are oriented with drive and sense sides swapped. This interleaving of drive and sense plus the effective lever arm allows the segment-to-segment height difference and dihedral angle to be algebraically separated. This “height” output part of the control geometry is identical to that of the Keck telescopes.

Besides the “height” signal, the TMT edge sensors also provide a “gap” signal, which enables segment in-plane positions to be calculated

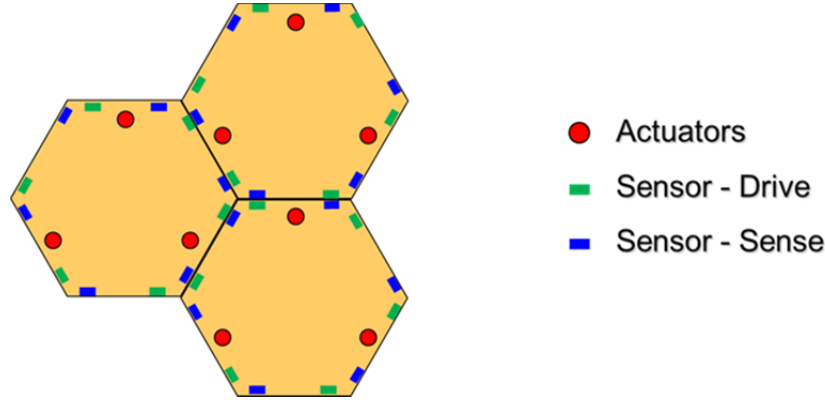


Figure 2. M1 Active Control Geometry. Drive and sense halves alternate along segment edges. This plus the sensor effective lever arm allow edge height difference and dihedral angle to be separated.

2.2 Segment and sensor coordinate definitions

Sensor locations are defined in segment coordinates. To account for sensor installation errors, each sensor half has a nominal position, and an actual position offset in six degrees of freedom from the nominal. For evaluating sensor readings, the two sensor halves also have a coordinate system relative to each other, which is fixed, in our convention, to the center of the sense half.

There are conventional names for some of this geometry. For example, a rotation around the sensor_x axis, that is, the segment edge, is called “ θ_x ” or “dihedral angle” or “tilt”. The distance from drive-side to sense-side along sensor-y is “gap”, and the mismatch along sensor-x is “shear”. The z difference is “piston” or “height”.

The nominal TMT segment gap is 2.5 mm. A 0.5 mm edge bevel makes the gap in the optical surface 3.5 mm. The nominal sensor drive-to-sense gap is larger, 4.8 mm, to provide clearance during segment exchange. The nominal sensor shear is zero. Flexure, temperature and installation tolerances combine to make both sensor gap and shear deviate from their nominals by +/- 0.9 mm maximum.

2.3 Focus mode and dihedral angle sensitivity

Focus mode is the first non-singular mode of the control model of M1. To first order it is a change in the radius of curvature of the surface defined by segment centers, with segment tilts such that neighboring segment edges remain lined up in height. Focus mode can be created, for example, by temperature change. Sensors that only see height find focus mode nearly unobservable, while sensors with dihedral angle sensitivity, that is, non-zero L_{eff} , have an error multiplier for focus mode inversely proportional to L_{eff} .

The plan for controlling M1 focus mode at TMT is to refocus the telescope by moving the secondary mirror (M2) to correct most of the wavefront error due to focus mode. The residual wavefront error after focus mode has been corrected by telescope refocusing is called scalloping. It is called scalloping because of the appearance of the surface error in cross section. The wavefront error from focus mode is reduced by a factor of $\sim N$ by refocusing M2, where N is the number of segments in M1. The input for the refocusing is the Acquisition, Guiding and Wavefront Sensing System (AGWFS), which updates M2 piston at least once every several minutes. Refocusing reduces the impact of focus mode enough for the edge sensors to meet TMT system requirements with easily attainable levels of L_{eff} .

2.4 The TMT capacitive edge sensor

In the TMT edge sensor geometry (Figure 3), there are two drive plates, driven with equal and opposite sine wave drive of about 6V amplitude. There is a single sense plate that sees an induced current proportional in sign and magnitude to any displacement from the plane of symmetry. The TMT capacitive sensor's face-on design allows segment exchange without moving sensor parts¹⁰. The analytic model used in the control simulations is summarized in Equation (1). The symbols used in Figure 3 and Equation (1) are defined in Table 1.

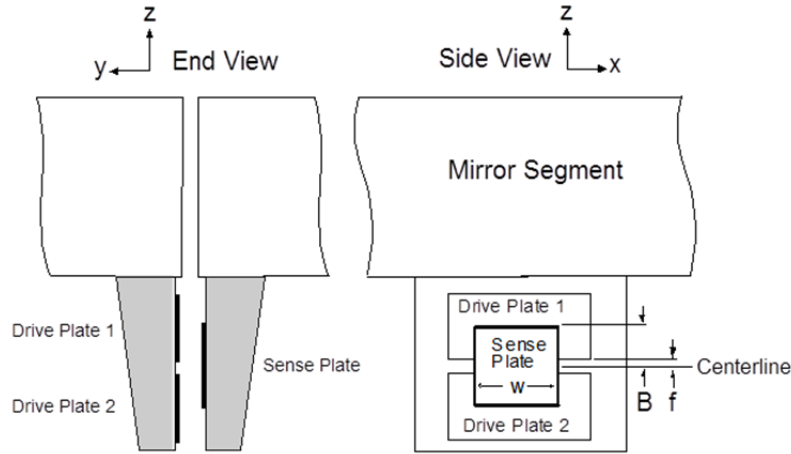


Figure 3. TMT Edge Sensor Geometry

Equation (1) describes the sensor “height” reading as a function of the position and orientation of the drive plate in a coordinate system fixed in the center of the sense plate. In the simulation model of the M1 control system, one transforms into this coordinate system to compute the sensor reading, taking into account sense-side and drive-side sensor installation errors, in-plane segment motion, and sensor flexure with gravity. The equation is valid for both sine and square wave excitation, with the units of the sensor reading being amperes for sine wave excitation, and coulombs for square wave excitation.

$$\begin{aligned}
 R &= \frac{A}{y} \left(k(B - f) - z - x\theta_y + \frac{B^2 - f^2}{2y} \theta_x \right) \\
 A &= \varepsilon_0 w V \quad \text{Square wave excitation} \\
 A &= 2\pi f_s \varepsilon_0 w V \quad \text{Sine wave excitation} \\
 L_{eff} &= \frac{B^2 - f^2}{2y}
 \end{aligned} \tag{1}$$

Equation (1) shows the mixed dependence of the “height” output of the sensor on true height, z , and on dihedral angle, θ_x . It also shows that the height and dihedral angle dependencies are proportional to two different powers of gap, y . The M1 Control System uses “gap compensation” to partially remove the gap dependence of the height reading. This is done by multiplying each sensor’s height reading by its gap reading to some power, as in Eq. (2). Setting power p to 1 is the baseline gap compensation. It is used in all cases presented in this paper. Setting p to 1.5 appears to improve calibration performance about 30%. This and other proposed gap compensation concepts may in the future improve calibration performance over that presented here.

Table 1. TMT Edge Sensor Properties.

R	Sensor reading (coulombs for square wave, amperes for sine wave)
ϵ_0	$8.854 \cdot 10^{-12}$ farads / meter
w	Sense plate effective width (30 mm)
2B	Sense plate effective height (45 mm)
2f	Effective spacing between drive plates (6 mm)
y	Gap from drive to sense (4.8 +/- 1.0 mm)
V	Drive amplitude (0 to 8.192 Vpp)
fs	Drive frequency (50kHz for height reading, 100kHz for gap reading)
θ_x, θ_y	Drive-side tip and clocking as seen from sense side
x, y, z	Coordinates of drive side origin as seen from sense side
k	(Common-mode drive amplitude) / (Differential drive amplitude)

The term k(B-f) in Equation (1) is a height offset term that comes from adjusting the balance of drive voltages on the two drive plates. It is used to offset each height reading to near zero as part of Alignment and Phasing System (APS) procedure. The magnitude of the offset in nanometers is referenced to the dimensions of gold electrodes deposited onto Zerodur, making the offset scaling stable and consistent across sensors. In this parallel-plate analysis, the offset in nanometers is independent of gap, with or without gap compensation.

$$R = \frac{gap^p}{A} \left(\frac{A}{gap} z + \frac{C}{gap^2} \theta_x \right) \quad (2)$$

The last line of Equation (1) is an expression for L_{eff} , the ratio of height sensitivity to dihedral angle sensitivity. It can be seen there and in Equation (2) that L_{eff} has a $1/gap$ dependence. The sense-to-drive spacing ranges from 3.9 to 5.7 mm, with 4.8 mm as the nominal gap. L_{eff} ranges from 42.9 mm at maximum gap to 65.4 mm at minimum gap, and is 51.8 mm at the nominal gap.

The largest contribution to gap variation is from segment installation errors, which are static and as much as a millimeter. Dynamic gap changes due to temperature and flexure are smaller.

3. CALIBRATION METHODOLOGY

3.1 Calibration procedure overview

The TMT Alignment and Phasing System (APS) aligns the segments and then phases them to get minimum wavefront error on M1¹⁷. The calibration procedure combines results of several APS runs obtained at different zenith angles and temperatures, fits them to a calibration model, and uses the model to maintain wavefront quality under all telescope operating conditions¹⁸. There are two parts to this process, a calibration phase and an observing phase. The calibration phase has this outline:

- Each APS run gives a set of “desired sensor readings” and sensor gap readings, which are saved to a calibration database.
- In the calibration database, sensor shear and segment in-plane positions are calculated from the gap readings and also saved.
- The coefficients in a fitting equation are fit to the collection of desired sensor readings, gaps and shears from all APS runs, and saved.

The observing phase has this outline:

- Run-time sensor shear is calculated from run-time sensor gap readings.

- The gap and shear data are put into the fitting equation with the saved calibration coefficients.
- The resulting corrections are applied to sensor height readings.
- The corrections are continuously computed and applied for each sensor as the telescope tracks an object, taking into account both changes in zenith angle and temperature.

3.2 Fitting functions

A fitting function computes a correction to sensor readings from fit coefficients times observables such as a gap, shear, 1/gap, gap_mean, zenith_angle.

The basic fitting function, used when fitting four or more APS runs, has a constant, a gap term and a shear term for each sensor, as seen in Eq.(3).

$$\text{Reading Correction} = C_0 + C_1 \Delta \text{gap} + C_2 \Delta \text{shear} \quad (3)$$

With one APS run, there is nothing to fit – the reading correction from the single APS run becomes the constant term C_0 , which is the only term. For two to four APS runs, specialized fit equations have been devised. The most important of these uses a “multiple baseline” technique. It gave better results than the baseline fitting function for 2 and 4 APS runs. In the “multiple baseline” procedure, each sensor can use a different APS run to treat as the baseline from which to compute delta gap and delta shear. The increased size of the database is the price paid for the improved fitting performance. This procedure deals with ill-conditioned matrices by inverting several possible matrices for each sensor and choosing the one with the lowest magnitude correction.

3.3 The magnitude of errors corrected

The sensor installation errors θ_x and θ_y combine with gap and shear in-plane motions to give rise to the largest error terms needing calibration. In the simulation, errors are evaluated rigorously using Equation 1 and proper 3D transformations, but the rough order of magnitude of the errors can be obtained by multiplying sensor installation errors θ_x and θ_y (in milliradians) by the magnitude of gap and shear motions (in micrometers) to estimate sensor offset error terms (in nanometers).

The current expected θ_x installation error for the TMT edge sensors is 0.5 mrad rms. In-plane motions from gravity, discussed in the next section, are typically 50 μm rms, 270 μm peak when changing zenith angle by 35 degrees. Multiplying installation error by the in-plane motion gives a sensor height reading error of 25 nm rms, 135 nm peak. This translates to an OPD error of 425 nm rms, or 2300 nm peak. The TMT requirements are much smaller than these, hence the need for a calibration procedure.

Sensor temperature coefficients are included in the simulation, using coefficient values up to 12 nm/C. This was the measured temperature coefficient of the April 2012 sensor electronics; subsequent modifications of the electronics have greatly reduced the temperature coefficient.

Sensor flexure with gravity can give up to 12 nm p-v of OPD, if not corrected. This small effect is essentially eliminated in calibration.

Non-spherical segments which are clocked or translated give a figure error, and an edge height difference of up to 150 nm. A simple model of warping is included in the simulation to account for the interaction this has with calibration.

3.4 In-plane motions due to gravity

In-plane sensor motions due to gravity are interpolated from an FEA-generated table of segment displacements and rotations. When computing the effect of gravity on sensor readings, interpolated segment motions are translated into sensor motions via standard rotation and translation matrices, and a sensor reading calculated using Equation (1). There are two FEA tables available; the newer, called “2010/10/22/ FEA” is the default and is used in this report’s simulations. The older, “2008 FEA”, is available for comparison.

The minimum, RMS and maximum in-plane motions that the 2772 edge sensors see due to gravity, relative to a baseline position at 30 degrees, is given in Table 2.

Table 2. Summary of Segment In-plane Motions Due to Gravity. These are relative motions of sensor drive as seen by sensor sense for 2772 sensors. Sensor-X (shear) is along the segment edge and sensor-Y is the gap dimension. Motions are relative to segment positions at 30 degrees zenith.

	Min (mm)	RMS (mm)	Max (mm)
Sensor-X, 0 degrees	-0.16	0.035	+0.13
Sensor-X, 65 degrees	-0.16	0.042	+0.19
Sensor-Y, 0 degrees	-0.21	0.040	+0.23
Sensor-Y, 65 degrees	-0.27	0.052	+0.20

3.5 In-plane motions due to temperature

While a more detailed thermal model can be incorporated in future work, for now we model only the effect of uniform temperature on the M1 support structure and thermal clocking of the individual segments.

“Thermal clocking” means individual segments rotate around their local Z-axis when the temperature changes. Thermal clocking is a consequence of the geometry of the segment attachments in the segment support assembly. In the interior of a sector, the effect of clocking on sensors is primarily a change in shear, while at the sector-sector boundaries, gap changes dominate.

Summarizing the specific assumptions currently used in the M1CS simulation:

- The telescope is at a uniform temperature;
- The segment centers undergo simple global thermal expansion at the temperature coefficient of expansion of steel, 11.6 ppm/C;
- Items fixed to the Zerodur segments move with the segment rigid body motion;
- Segments undergo thermal clocking at $6.8 \mu\text{rad}/\text{C}$, in a direction that depends on sector. The segments in sectors A,C,E clock in positive θ_z , where z is the segment center skyward normal. The segments in sectors B,D,F clock in negative θ_z .

3.6 Sensor gravity deformation

The deformation of the edge sensor halves under their own weight was evaluated using finite-element analysis, and confirmed with laboratory measurements. The result was modeled as a rigid-body rotation of $2.25 \mu\text{rad}$ when moving from zenith to horizon, for sensors on an edge parallel to the elevation axis. The effective pivot axis lies in the plane of the sensor mounting feet.

Sensor flexure results in an OPD of 12 nm peak-to-valley when going from 30 deg to 65 deg zenith angle, without a calibration procedure. The calibration procedure reduces this effect to a negligible level.

3.7 The interaction of warping and calibration

Clocking a segment about its own z-axis generates no optical error if the segment is spherical, but can generate significant local astigmatism if the segment is appreciably aspherical. Figure 4 illustrates this for the case of segment clocking due to segment installation errors at the level expected for TMT. The colors represent surface error, spanning -150 nm to +150 nm. There is no surface error in the center of the primary mirror, but there is appreciable surface error at its rim.

Installation errors are static errors, and the segment warping procedure removes the bulk of this error, at one zenith angle and temperature. What remains is the thermal clocking already mentioned, and some clocking that happens with gravity flexure. The calibration procedure then compensates for these dynamic changes at other zenith angles and temperatures.

There is an operational assumption here that after a segment exchange, warping is done once, under the guidance of the APS, at a representative zenith angle and temperature, and not done again while APS runs are

performed at other zenith angles and temperature as part of the calibration procedure. The reason for this is that sensors are attached to segment edges, and their position in segment coordinate system changes with warping. Thus, re-warping implies re-calibrating.

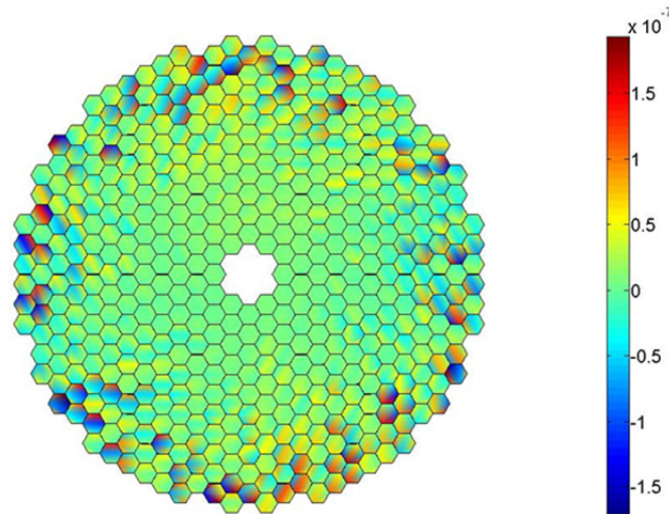


Figure 4. Surface Error from Segment Clocking due to Segment Installations Errors. The span of the colorbar is -150 to +150 nm.

If it is desired to warp segments without an accompanying APS run, an accurate model of the effect of warping commands on sensor readings must be constructed. Such a model will also be needed if it is desired to track long term secular drifts in sensors. Otherwise, sensor offset history is erased with each warping operation.

4. CALIBRATION METHODS

4.1 The 6 Degree-of-Freedom A-matrix

The 6DOF A-matrix expresses how segment motions in all six degrees of freedom affect edge sensor height, gap and shear. The 6 DOF A-matrix is the heart of the M1CS simulation, and plays a major role in analyzing calibration, control stability and focus mode, in comparing alternative sensing methodologies, and is necessary for the gap-to-shear transformation.

To give as realistic a simulation of M1 as possible, the 6DOF A-matrix has a full set of input parameters. These are:

- Correct basic geometry (right focal length, conic constant)
- Merit-Function-generated segment, vertex, sensor and actuator locations and orientations
- Gravity deformations from FEA
- Thermal expansion
- Thermal clocking
- Segment installation error
- Sensor installation error
- Sensor gravity flexure
- Sensor temperature coefficient

Physically, the 6 DOF A-matrix is a set of Matlab routines that implement a rigorous 3-D model of the M1 geometry for controls analysis. The routines calculate the coefficients in the interaction matrix, or A-matrix, that connects drive-to-sense height, gap and shear values of all edge sensors to the positions and orientations of all segments. Equation (4) illustrates the 6DOF A-matrix relationship in matrix notation.

$$\begin{pmatrix} height \\ gap \\ shear \end{pmatrix} = A_{6DOF} \begin{pmatrix} tip \\ tilt \\ piston \\ inplane_X \\ inplane_Y \\ clocking \end{pmatrix} \quad (4)$$

4.2 Computing shears from gaps

Calibration requires knowledge both of gap and shear aspects of the in-plane segment motions. The TMT baseline sensor provides a gap output, but not a shear output.

Shear data can be measured with shear sensing (ESO approach), or computed from gap data (TMT approach). The procedure for computing shears from gaps has been described by Chanan¹⁹ and is summarized here.

Gap readings, called $y_{measured}$ here, can be turned into best-fit sensor $x_{calculated}$ (shear) and $y_{calculated}$ (gap) offsets as follows –

$$\begin{aligned} x_{calculated} &= HG^{\dagger} y_{measured} \\ y_{calculated} &= GG^{\dagger} y_{measured} \end{aligned} \quad (5)$$

G is the matrix connecting segment in-plane coordinates to sensor gap and shear. G^{\dagger} is the pseudo-inverse of G. H connects segment in-plane coordinates to sensor gap and shear. Both G and H are extracted from the 6DOF A-matrix.

The gap-to-shear procedure works well, and has the side benefit of filtering out the unphysical part of gap noise. In simulation, the measured noise multiplier agrees with the theoretical value.

4.3 Torsion mode

There is one unobservable mode, “torsion mode”, which is lost in computing shear from gap²⁰. It is essentially the mean clocking of all segments.

Because of its symmetry, the complete M1 shows very low mean clocking of segments. However, with one missing segment, for example, there is mean clocking of (6.8/492) $\mu\text{rad/C}$. Estimating the consequences of this awaits modifying the simulation to model an incomplete M1, with missing segments or rings of segments. This is planned future work.

If torsion mode does need to be observed, a single or a very few shear sensors are sufficient to bring the torsion mode noise multiplier in line with other modes²¹.

Adding shear sensing to the current edge sensor design would require modifying the drive side and firmware only. The resulting shear-capable drive-side assembly would be a drop-in replacement. There would be no sense-side or cabling changes. The added cost to do this for one or a few edge sensors is low.

5. SIMULATION OF M1CS AND CALIBRATION

A set of simulation and diagnostic programs have evolved in response to the need to fully analyze the calibration issue. The result of this evolution is the M1CS Simulation, which unifies previously separate calibration and A-matrix codes, and connects tightly with TMT databases and FEA modeling.

It is a time-domain simulation of the M1 Control System, capable of modeling non-linear effects such as sensor and actuator saturation, in which the positions and orientations of all M1CS elements are tracked, with rigorous handling of all rotations and translations.

The intent is that these routines evolve into the deliverable Matlab routines to the Global Loop Controller (GLC) effort. Some pieces will become actual GLC code, and some pieces will become telescope simulation stubs for GLC code.

Some features of the simulation code are:

- The M1CS simulation model imports irregular segments from the TMT Segmentation Database. Sensor and actuator locations are also imported, in 3D, rather than calculated.
- All math is fully general, with no small angle approximations. Full 3x3 rotation matrices are used.
- The full 6DOF A-matrix is evaluated.
- The 6DOF A-matrix enables computing shears from gaps for the 3D mirror with irregular hexagons.
- It allows comparison between different sensing and control techniques.
- For modeling gravity deformations, 2010/10/22 FEA data imported in a true 3D format can be selected, or 2008 FEA data imported in a 2D projection.
- It simulates closed loop feedback from an optical sensor, with a selectable number of zernike aberrations. For this presentation, simulations include correction of Zernike/Noll modes 4 through 11 unless stated otherwise.
- It models thermal clocking of segments
- It models sensor flexure and sensor temperature coefficient
- It accurately simulates closed loop behavior of the M1CS, including any non-linear effects.

Figure 4, already shown, is a display from the simulation showing M1 surface error after an APS alignment and phasing run, but before the warping harnesses are adjusted. Surface errors range from -150 to +150 nm.

6. PARAMETRIC STUDIES

In this section we present the significant results of the calibration simulation. These are parametric studies that use the simulation to evaluate calibration performance as a function of several important system parameters. These are sensor installation errors, the number and diversity of APS runs, sensor temperature coefficient, and sensor correlated drift.

6.1 Quantifying calibration performance using PSSN

The figure of merit for evaluating calibration performance is Point Source Sensitivity, Normalized, or PSSN^{22,23}. This is the figure of merit chosen by TMT for quantifying telescope performance for all seeing-limited observations. It ranges from 0 to 1, with 1.0 being the best a system can achieve. PSSNs have the useful property that PSSNs from different error sources combine by multiplying their individual PSSN contributions.

“Calibration Error”, or “Calibration PSSN” is the ratio of two PSSNs; the first is PSSN calculated with desired sensor readings created from the calibration procedure, the second is PSSN calculated with desired sensor readings fully optimized for the observing zenith angle and temperature.

The TMT PSSN specification for all error sources combined is 0.85. This overall PSSN allocation is the product of PSSN allocations for individual error sources. The PSSN allocation for calibration incorporates four effects, with these current allocations in the error budget

- APS noise 0.9955,
- “Sensor Calibration” 0.998,
- Thermal clocking: 0.99984 ($\Delta T = 4K$),
- Decenter: 0.99956 (moving from 30 to 60 deg zenith angle)

The product of these is PSSN = 0.9929. In the simulations that follow, we use this number to be the threshold for requirement compliance for “Calibration Error”, or “Calibration PSSN”.

6.2 Standard Year Weighting

The TMT Standard Year is a three-year record of Mauna Kea temperatures and Gemini North pointing which is considered representative of what TMT will be doing²³. “Standard Year Weighting” is a two-dimensional weighting function, derived from the Standard Year record, for averaging any telescope performance metric over zenith angle and temperature. In this document, it will be applied to PSSN, to create a Standard Year Averaged PSSN as a single figure of merit for use in the TMT optical error budget.

6.3 Use cases

In addition to having a standard weighting over zenith angle and temperature, the parametric studies use a standard set of APS runs. The convention for the parametric studies is that when N APS runs are called for, APS runs 1 through N are used, from this standard set.

APS run 1 has special status. It is intentionally placed at the peak of the probability distribution, namely, 30 degrees zenith angle and +3 C temperature. It is assumed that this is always the first APS run, and that warping is applied here and is not adjusted thereafter.

6.4 Default values of parameters

Table 3 lists default values for the parameters relevant to the calibration parametric studies.

Other parameters in the simulation not listed here proved useful in verifying algorithms and in understanding cause and effect in the complex MICS system. For example, it was useful to be able to set the conic constant of M1 to zero, to show that many of the problems of clocking segments go away if M1 is spherical. It was also useful to make the focal length of M1 many kilometers, to see how curved mirror singular values approached flat mirror singular values.

Table 3 Default Values of Parameters

Parameter	Value
Segment Install Errors	$\sigma_x = 200 \mu\text{m}$ $\sigma_y = 200 \mu\text{m}$ $\sigma_z = 200 \mu\text{m}$ $\sigma_{\text{clocking}} = 285 \mu\text{rad}$
Sensor Install errors	Nominals: $\sigma_{\theta_x} = 0.5 \text{ mrad}$ $\sigma_{\theta_y} = 0.3 \text{ mrad}$ Parametric scan: $\sigma_{\theta_x} = \sigma_{\theta_y} = 0.2, 0.5, 1.0, 2, 3 \text{ mrad}$
Sensor Noise for Calibration Purposes	$\sigma_h = 1 \text{ nm rms}$ $\sigma_g = 300 \text{ nm rms}$
APS Noise	Modeled as 10.4 nm rms random error in desired sensor readings.

6.5 Calibration error vs installation error

Figure 6-1 shows the Standard-Year-averaged PSSN achieved during observations as a function of the magnitude of edge sensor installation errors. The specific sensor installation error plotted is a tilt about an axis parallel to the segment edge (θ_x), in milliradians. In the simulation, the θ_y and θ_z installation errors are scaled proportionally with the θ_x value.

For small installation errors, the calibration PSSN asymptotes to a value set by APS noise. PSSN degrades less than 0.002 from the APS asymptote for expected installation errors, consistent with requirement.

The sensor installation specification of 0.5 mrad rms is indicated on the figure. Without calibration, the requirement for sensor installation would be approximately 20x more stringent.

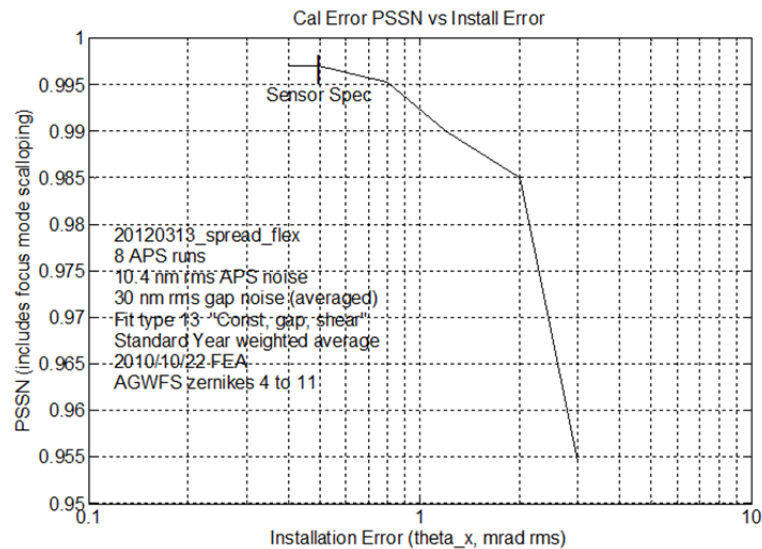


Figure 6-1 Calibration PSSN vs Sensor Installation Error

6.6 Calibration error vs number of APS runs

Minimizing the number of APS runs required to properly calibrate the telescope is a key to operational efficiency. Figure 6-2 shows the Standard Year Weighted PSSN achievable during observations as a function of the number of APS runs that went into the calibration. Standard Year weighting over zenith angle and temperature is used, and the zenith angles and temperatures are from the standard Use Cases.

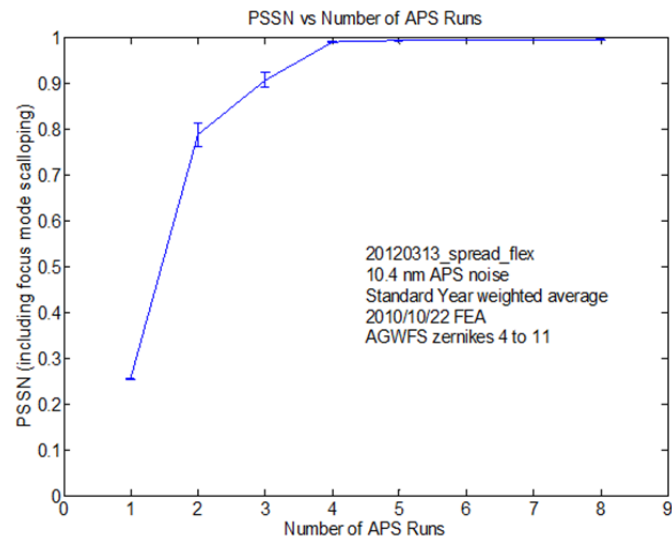


Figure 6-2 Calibration PSSN vs Number of APS Runs

The vertical bars show the spread in results when different random seeds are used in the simulation. Any parameter values not annotated have their default values.

The average PSSN rises above the required 0.993 for 5 APS runs or more. This and the previous figure show that APS runs with sufficient diversity of zenith angle and temperature are required for complete calibration over all zenith angles and temperatures.

Figure 6-3 shows contour plots of calibration PSSN versus zenith angle and temperature for one through eight APS runs. The APS runs of the standard Use Cases are shown as white circles.

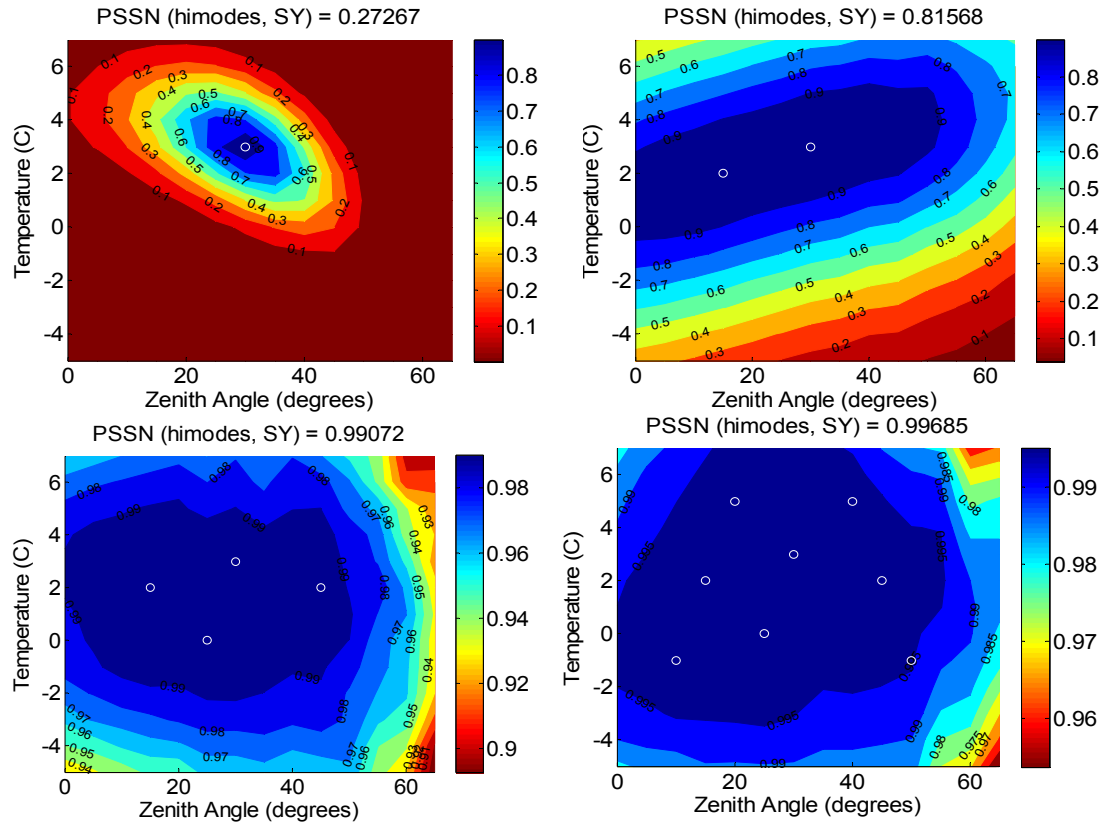


Figure 6-3 Calibration PSSN vs Zenith Angle and Temperature for 1, 2, 4, 8 APS Runs. The Standard Year Averaged PSSN ranges from 0.273 to 0.997, as notated on the plots.

6.7 The PSSN impact of sensor temperature coefficient

A temperature coefficient was added to the standard sensor model, and PSSN vs installation error was evaluated. With 12 nm/C sensor temperature coefficient, much larger than is currently observed, the PSSN impact of sensor temperature coefficient was 0.997. We conclude that the calibration procedure is robust without modification against attainable sensor temperature coefficients.

6.8 The PSSN impact of sensor gravity deformation

Sensor flexure is included in the baseline model, using a flexure model developed from FEA and verified by lab measurements, as described in Section 3.6. The model shows 12 nm peak-to-valley OPD that results from sensor flexure when going from 30 deg to 65 deg zenith angle, without a calibration procedure. The calibration procedure reduces this OPD error to a negligible level. The resulting reduction in Standard Year averaged PSSN due to sensor flexure is very small, about 0.0001.

6.9 The PSSN impact of correlated sensor drift

There are separate considerations for height drift, which impacts focus mode directly, and gap drift, which is a less serious system issue.

Any collective drift, caused either by temperature or aging, of all edge sensor height readings moving together maps directly to focus mode, with a high multiplier. For example, +1.0 nm collective drift of all edge sensors together gives an rms OPD of ~850 nm.

The zernike focus portion of this is removed by pistoning M2 to refocus the telescope, under control of the Acquisition, Guiding and Wavefront Sensing System (AGWFS). The residual after this refocusing is called “scalloping”, because of the appearance of the residual in cross-section.

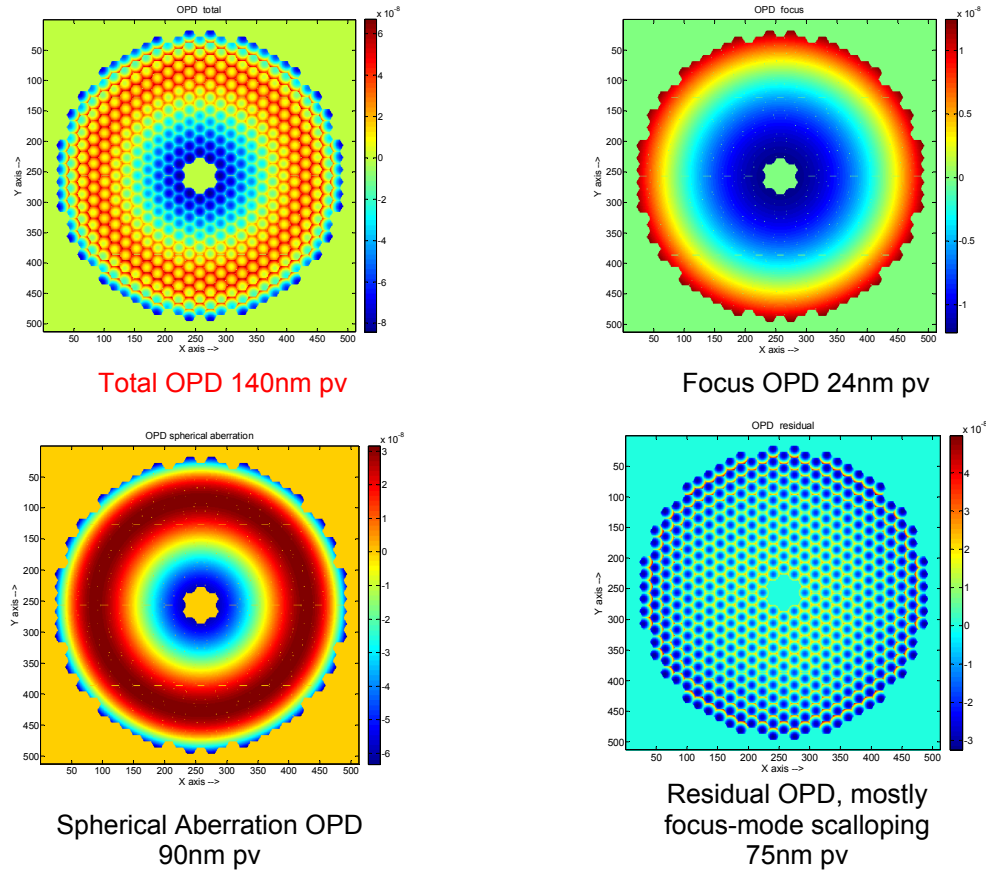


Figure 6-4 OPD for 1 Micron of M1 Focus Mode Corrected with M2 Piston. This corresponds to about 1.1 nm correlated sensor drift.

Figure 6-4 shows the decomposition of the residual OPD after refocusing M2 to correct 1 micron of M1 focus mode, or about 1.1 nm correlated sensor drift. The total OPD is 140 nm peak-valley, which decomposes into 24 nm of zenike focus, 90 nm p-v of spherical aberration, and 75 nm p-v of scalloping.

Table 4 summarizes the statistics of correcting correlated sensor drift of the height signal by M2 refocus. Notice the low-order zernikes have much less impact on PSSN than scalloping for the same OPD.

The effect of sensor correlated drift in the gap signal was simulated by adding an offset to the gap signal and evaluating the impact on PSSN. The impact on PSSN was minimal: 5 μm of gap signal offset had a PSSN impact of 0.9988. The gap signal offset is expected to be small compared to 5 μm .

Table 4 OPD and PSSN from ~2.0 nm Correlated Sensor Drift

Parameter	No Refocus	M2 Refocus
M2 piston, microns	0.0	-57.3
Focus OPD, rms nm	1834	0.3
Focus PSSN	0.86	1.0000
Spherical aberration OPD, rms nm	-17.9	9.7
Spherical aberration PSSN	0.99999	1.0000
Scalloping OPD, rms nm	4.7	4.6
Scalloping PSSN	0.9994	0.9994
Total OPD, rms nm	1837	10.7
Total PSSN	0.86	0.9994

7. CONCLUSIONS

We have defined and fully simulated a calibration procedure for the TMT M1 Control System, and have shown that M1CS can meet its requirements with attainable sensor installation errors. We conclude that the approach of using gap sensing plus multiple APS runs to calibrate the face-on sensor to correct for in-plane motion and other effects has been validated.

As new error sources have been identified and added to the simulation, such as sensor sag with gravity, and sensor drift with temperature, the procedure has proven robust against these too, without needing modification.

After a segment exchange, only three APS runs at different zenith angles are necessary for good performance. Additional APS runs can be added over time to achieve good performance over the full extent of the TMT operational environment including temperature extremes. The current simulation assumes all segments have the same number of APS runs. In the future, a more realistic simulation will be developed that will bookkeep different APS histories for different segments.

ACKNOWLEDGMENTS

This research was carried out at the Jet Propulsion Laboratory, California Institute of Technology, which is operated by Caltech for the National Aeronautics and Space Administration. The TMT Project gratefully acknowledges the support of the TMT collaborating institutions. They are the Association of Canadian Universities for Research in Astronomy (ACURA), the California Institute of Technology, the University of California, the National Astronomical Observatory of Japan, the National Astronomical Observatories of China and their consortium partners, and the Department of Science and Technology of India and their supported institutes. This work was supported as well by the Gordon and Betty Moore Foundation, the Canada Foundation for Innovation, the Ontario Ministry of Research and Innovation, the National Research Council of Canada, the Natural Sciences and Engineering Research Council of Canada, the British Columbia Knowledge Development Fund, the Association of Universities for Research in Astronomy (AURA) and the U.S. National Science Foundation..

REFERENCES

For TMT internal documents see tmt.org/documents or contact inquiry@tmt.org.

- [1] F. Shi, G. Chanan, C. Ohara, M. Troy & D.C. Redding, "Experimental verification of dispersed fringe sensing as a segment phasing technique using the Keck telescope", *Apl. Opt.* **43**, 4474–4481 (2004).
- [2] S. Esposito, E. Pinna, A. Puglisi, A. Tozzi, & P. Stefanini, "Pyramid sensor for segmented mirror alignment", *Opt. Letters* **30**, 2572–2574 (2005).
- [3] F. Hénault, "Multi-spectral piston sensor for co-phasing giant segmented mirrors and multi-aperture interferometric arrays", *J. Opt. A: Pure Appl. Opt.* **11**, 125503 (2009).
- [4] R.H. Minor, A.A. Arthur, G. Gabor, H.G. Jackson & R.C. Jared, "Displacement sensors for the primary mirror of the W.M. Keck Telescope", *Proc. SPIE* **1236**, 1009–1017 (1990).
- [5] P. Palunas, J.R. Fowler, J.A. Booth, G. Damm & G.H. Ames, "Control of the Hobby-Eberly Telescope Primary Mirror Array with the Segment Alignment Maintenance System", *Proc. SPIE* **5496**, 659–666 (2004).
- [6] D. Rozière, S. Buous, A. Courteville, "Position sensor for segmented mirror", *Proc. SPIE* **5495**, 660–669 (2004).
- [7] R. Gilmozzi & J. Spyromilio. "The 42m European ELT: Status", *Proc. SPIE* **7012**, 701219–701219-10 (2008).
- [8] J. Nelson & G. H. Sanders, "The status of the Thirty Meter Telescope project," *Proc. SPIE* **7012**, 70121A–70121A-18 (2008).
- [9] M. Johns, "Progress on the GMT", *Proc. SPIE* **7012**, 70121B–70121B-15 (2008).
- [10] T. Mast, G. Chanan, J. Nelson, R. Minor, & R. Jared, "Edge sensor design for the TMT", *Proc. SPIE* **6267**, 62672S–62672S-15 (2006).
- [11] D. Rozière, B. Luong, B. Fuchs, A. Périn, C. Néel, S. Lévêque, "Inductive edge sensors: an innovative solution for ELT segmented mirror alignment monitoring", *Proc. SPIE* **7012**, 701217–701217-14 (2008).
- [12] D.A.H. Buckley, S. Buous, H. Gajjar, J.W. Menzies, F. Schindler, K. Sändig & S. Lévêque, "A novel optical sensor for mirror edge sensing", *Proc. SPIE* **7739**, 773912–773912-14 (2010).
- [13] D. G. MacMartin, G. A. Chanan, "Control of the California Extremely Large Telescope primary mirror", in *Future Giant Telescopes*, R. J. Angel and R. Gilmozzi, eds., SPIE 4840, pp. 69-80, 2003.
- [14] Chanan, G., MacMartin, D.G., Nelson, J., and Mast, T., "Control and Alignment of Segmented-Mirror Telescopes: Matrices, Modes and Error Propagation", *Applied Optics*, **43**, 1223-1232 (2004).
- [15] MacMartin, D.G., and Chanan, G. "Measurement Accuracy in Control of Segmented-Mirror Telescopes", *Applied Optics*, **43**, 608-615 (2004).
- [16] Roberts, S., Sun, S., Kerley, D., "Optical performance analysis and optimization of large telescope structural designs", *Proc. SPIE* **5867**, 200-211 (2005).
- [17] G. Chanan, M. Troy, I. Crossfield, J. Nelson, and T. Mast, "The Alignment and Phasing System for the Thirty Meter Telescope," *Proc. SPIE* **6267**, pp. 62672V (2006).
- [18] Shelton, C., Mast, T., Chanan, G., Nelson, J., Roberts, L., Troy, M., Sirota, M., Seo, B-J., MacDonald, D., "Advances in Edge Sensors for the Thirty Meter Telescope Primary Mirror", *Proc. SPIE* **7012**, 35 (2008).
- [19] Gary Chanan, "Segment In-Plane Position Sensing", TMT.CTR.PRE.07.019.REL01 (2007).
- [20] J. Nelson, "Edge Sensors: Abstract view," TMT.PSC.PRE.07.004.DRF01 (2007).
- [21] MacMynowski, D. G., Roberts Jr., L. C., Shelton, J. C., Chanan, G. and Bonnet, H. "In-plane effects on segmented mirror control", *Applied Optics*, **51**(12), pp. 1929-1938 (2012).
- [22] B.-J. Seo, C. C. Nissly, G. Angeli, B. Ellerbroek, J. Nelson, N. Sigrist & M. Troy, "Analysis of normalized point source sensitivity as a performance metric for the Thirty Meter Telescope", *Proc. SPIE* **7017**, 70170T–70170T-12 (2008).
- [23] Seo, B.-J., Nissly, C., Angeli, G., Ellerbroek, B., Nelson, J., Sigrist, N., and Troy, M., "Analysis of Normalized Point Source Sensitivity as performance metric for large telescopes," *Applied Optics* **48**, pp. 5997–6007 (2009).
- [24] Vogiatzis, K., "Probabilistic Performance Analysis 'Standard Year'", TMT.SEN.PRE.07.030.DRF01 (2007).